



Selective synthesis of rhodium-based nanoframe catalysts by chemical etching of 3d metals†

Zhi-Ping Zhang, Wei Zhu, Chun-Hua Yan and Ya-Wen Zhang*

Cite this: *Chem. Commun.*, 2015, 51, 3997Received 17th December 2014,
Accepted 21st January 2015

DOI: 10.1039/c4cc10050f

www.rsc.org/chemcomm

We demonstrate a general strategy for the highly selective synthesis of Rh-based multi-metallic nanoframes through preferential etching of 3d metals, including Cu and Ni. Compared with Rh–Cu nanooctahedrons/C, Rh–Cu nanooctahedral frames/C show greatly enhanced activity toward hydrazine decomposition at room temperature.

Noble metal nanomaterials with unique chemical and physical properties have attracted decades of broad interests due to their promising applications in various fields such as photonics,¹ sensing,^{2,3} and catalysis.^{4–6} In particular, noble metal nanocatalysts are widely used in industrial catalysis, environmental remediation, and renewable energy processing; however, their large-scale and economical utilization is limited by the high cost of noble metals because of their scarce elemental abundance in the earth. Therefore, there is strong demand for the development of an atomically efficient approach for the synthesis of high-performance noble metal nanocatalysts with high activity, selectivity and durability but at low consumption of noble metals.

In recent years, several common strategies have been developed to achieve highly efficient and low-cost noble metal nanocatalysts. For instance, the shape control of noble metal based nanocrystals tunes the catalytic activity and selectivity by preferentially exposing efficient reaction sites (*e.g.*, high Miller index facets).^{7,8} Moreover, alloying noble metals with light transition metals can not only reduce the precious metal content, but can also elevate the reactivity of the nanocatalysts.^{9–11} In particular, building open structures, such as hollow,¹² porous structures¹³ or nanoframes (decahedral,¹⁴ cubic,¹⁵ octahedral,¹⁶ dodecahedral¹⁷), has drawn increasing attention because nanoparticles (NPs) with high surface areas can supply reactants with molecular accessibility and possess high atom utilization efficiency. To date, metal nanoframes have been obtained by a

few wet chemistry approaches, including one-pot methods,^{15,18} templating methods with galvanic replacement or Kirkendall effect,^{12,16,19} and etching methods through preferential corrosion of the less-noble metal elements for multi-metallic NPs with alloys^{17,20} or core–shell structures.^{14,21} Monometallic Au,^{14,22} Pt,²³ and multi-metallic Pt–Pd,¹⁹ Pt–Cu,^{15,18} Au–Ag,¹⁶ Pt–Ni,^{17,20} and Au–Pt–Ni²⁰ nanoframes were prepared by these strategies and displayed noteworthy material properties.

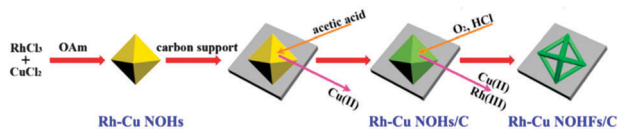
Rh-based catalysts are widely applied in heterogeneous and homogeneous catalysis.²⁴ Amongst the platinum group metals, rhodium is on the top rank of the rarest and the most expensive ones worldwide. Therefore, it is essential to look for novel high-performance Rh-based nanocatalysts with the lowest Rh content. Developing robust framework-like Rh-based catalysts will surely be a feasible way to achieve the abovementioned objective with a high-efficiency utilization of Rh resources. To date, only a limited number of studies have been reported for the syntheses of Rh-based nanoframes.^{21,25,26} These syntheses required the oxidative corrosion of noble metal Pd cores, which served as the sacrifice templates. For example, Rh cubic nanoframes were synthesized by removing the Pd core from Pd–Rh bimetallic nanocubes with a core–frame concave structure.²¹

In this communication, we report on a general approach for the highly selective synthesis of Rh-based (including Rh–Cu, Rh–Ni and Rh–Pd–Cu) nanoframes by employing 3d metals (*i.e.* Cu and Ni) as the sacrifice agents. Due to their open structure with more active Rh sites exposed and high molecular accessibility throughout the porous structure, the Rh–Cu nanoframes showed much faster hydrazine decomposition reaction rates than their solid counterparts and the as-prepared Rh/C at room temperature.

As shown in Scheme 1, we first synthesized monodispersed Rh–Cu nanooctahedrons (NOHs) *via* an oleylamine (OAm)-mediated solvothermal route (see Experimental section in the ESI†), then prepared Rh–Cu NOHs/C by using acetic acid (HAc) to clean their surfaces after loading the NPs on to carbon black. Taking advantage of the differences in resistance to oxidative corrosion between Rh and Cu by O₂/HCl, we finally converted Rh–Cu NOHs/C to Rh–Cu nanooctahedron frames/C (NOHFs/C) *via* a preferential etching of Cu in hot HCl solution.

Beijing National Laboratory for Molecular Sciences, State Key Laboratory of Rare Earth Materials Chemistry and Applications, PKU-HKU Joint Laboratory in Rare Earth Materials and Bioinorganic Chemistry, College of Chemistry and Molecular Engineering, Peking University, Beijing 100871, China.
E-mail: ywzhang@pku.edu.cn

† Electronic supplementary information (ESI) available: XRD patterns, more TEM images and other data. See DOI: 10.1039/c4cc10050f



Scheme 1 Synthetic protocol of Rh–Cu Nanooctahedrons (NOHs) and Rh–Cu Nanooctahedral frames/C (NOHFs/C).

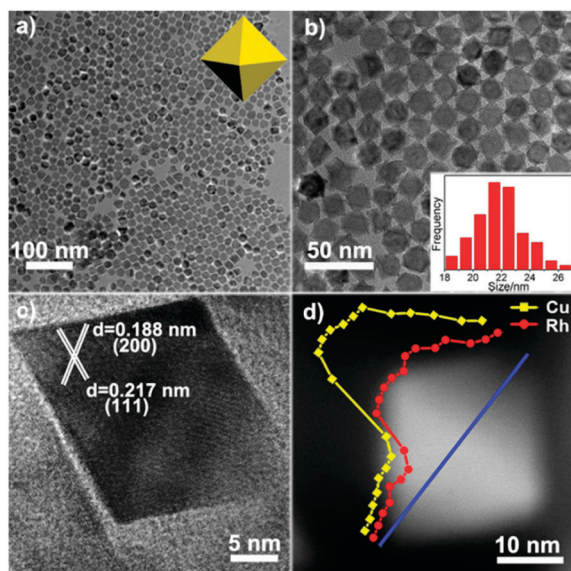


Fig. 1 TEM image (a) and magnified TEM image (b) of Rh–Cu NOHs. HRTEM image (c) and EDS line scan profiles (d) of Rh–Cu NOHs. Inset in panel b is the size distribution histogram of Rh–Cu NOHs.

The transmission electron microscopy (TEM) image (Fig. 1a) and magnified TEM image (Fig. 1b) show that Rh–Cu NOHs sized 21.9 ± 4.3 nm were prepared *via* the co-reduction of RhCl₃ and CuCl₂ using OAm as both the solvent and the reductant at 180 °C. The X-ray diffraction (XRD) pattern of the Rh–Cu NOHs exhibited three main peaks belonging to (111), (200), and (220) planes in turn, agreeing with the standard data of fcc Rh and Cu (Fig. S1, ESI[†]). As shown in the high-resolution TEM (HRTEM) image of Rh–Cu NOHs (Fig. 1c), the lattice fringes showed inter-planar distances of 0.217 nm and 0.188 nm, corresponding to the (111) and (200) planes, respectively. The value of 0.217 nm falls in between 0.220 nm for the fcc Rh(111) and 0.209 nm for the fcc Cu(111), indicating the formation of Rh–Cu alloy. As illustrated in the TEM images with different incidence directions, the shape of these NPs was of octahedron enclosed with eight (111) facets (Fig. S2, ESI[†]). The molar ratio of Rh/Cu in the NOHs was further determined to be 37:63 by inductively coupled plasma-atomic emission spectrometry (ICP-AES) analysis. In addition, high-angle annular dark-field scanning transmission electron microscopy-energy dispersive X-ray spectroscopy (HAADF-STEM-EDS) line scan analysis was used to analyze the distribution of Rh and Cu in a single Rh–Cu NOH. Fig. 1d shows an inhomogeneous elemental distribution in the NOHs. The segregation of Rh species on the surface of Rh–Cu NOHs was observed.

Rh–Cu NOHs were loaded on carbon black under ultrasonic treatment to prevent the NPs from aggregating. Subsequently, the carbon supported Rh–Cu NOHs were treated in HAC to remove most

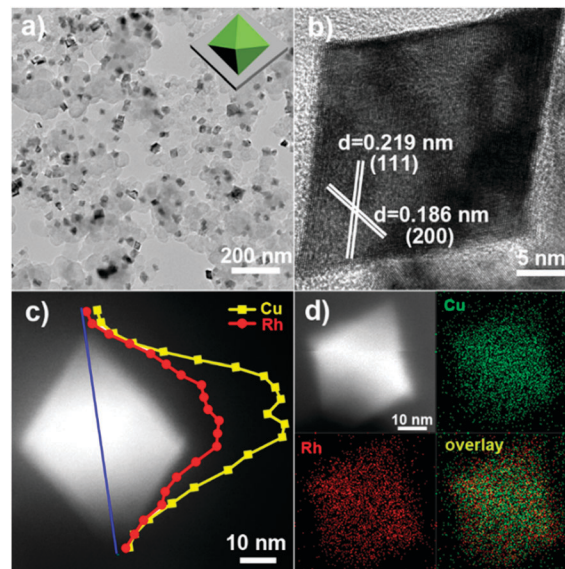


Fig. 2 TEM image (a), HRTEM image (b), EDS line scan profiles (c), and EDS elemental mapping images (d) of Rh–Cu NOHs/C.

of the capping agents of OAm on the surfaces (Fig. 2a),²⁷ as evidenced by the appearance of a very weak absorption peak of an N–H stretching vibration (*ca.* 3300 cm⁻¹ in Fig. S3, ESI[†]), together with a weak signal of an N 1s peak (*ca.* 398 eV in Fig. S4a, ESI[†]) in the X-ray photoelectron spectroscopy (XPS) spectra after the treatment. Moreover, small doses of Cu on the surfaces were leached during the HAC treatment process, as the Rh/Cu molar ratio in NOHs/C increased from 37:63 to 43:57, and the main XRD peaks shifted a little to the lower angle (Fig. S1, ESI[†]). The inter-planar distances of the lattice fringes were essentially unchanged, and the morphology had no evident change (Fig. 2b). EDS line scan profiles (Fig. 2c) and elemental mapping images (Fig. 2d) show that more Rh was enriched on the surface of the NOHs, compared with the interior of the NPs. The XPS result (Rh/Cu = 72:28) vs. the ICP result (Rh/Cu = 43:57) further illustrated the enrichment of Rh on the surfaces after HAC treatment. After OAm was washed off from the NP surfaces, a large fraction of surface Rh without the surfactant was oxidized because of the instability of the nanosized Rh particles, as revealed by the XPS results shown in Fig. S5a (ESI[†]). While copper was mainly distributed in the interior of the NPs, the valence of copper was zero under the protection of the surface Rh atoms, thus the 2p_{3/2} peaks corresponded to Cu⁰ (Fig. S5b, ESI[†]).

Oxidative etching in the presence of oxygen and proper coordination ligands (such as oleylamine,¹⁷ halogen ions²⁸ and dimethylglyoxime²⁹) offers a versatile route to transform the composition and the shape of metal nanocrystals. Furthermore, acid leaching is also a facile approach to control the formation of nanoporous or concave structured metals.³⁰ Compared with Rh ($\varphi^0\text{Rh(III)}/\text{Rh(0)} = 0.76$ V vs. RHE), Cu ($\varphi^0\text{Cu(II)}/\text{Cu(0)} = 0.34$ V) has a lower reduction potential, thus Cu atoms are more susceptible to being oxidized than Rh atoms in HCl solution in the presence of dissolved oxygen, and the selective etching reactions are given as follows:



As shown in Fig. S6 (ESI[†]), Rh tends to segregate at the edges and surface layers of Rh–Cu NOHs, as with the case of Pt in Pt–Ni octahedrons³¹ and Pt–Ni polyhedrons.¹⁷ When Cu atoms were etched, a small portion of Rh atoms was also removed from the Cu rich regions. Due to the segregation of Rh species on the edges, the atoms on the edges were barely dissolved; therefore, the NPs could retain their nanooctahedral frameworks, as illustrated in Fig. 3 and Fig. S7 (ESI[†]). After etching with HCl solution in air, the main XRD peaks of the NOHFs/C shifted further to the lower angle with reduced crystallinity (Fig. S1, ESI[†]), which was caused due to the increased lattice spacing and the destruction of the crystals (Fig. 3b), owing to the majority of Cu atoms being dissolved. Furthermore, the molar ratio of Rh/Cu was greatly increased from 43 : 57 to 73 : 27. The elemental mapping images (Fig. 3c) and HAADF-STEM-EDS line scan profiles (Fig. 3d) show the hollow structure for NOHFs/C. The XPS result (Rh/Cu = 88 : 12) vs. the ICP result (Rh/Cu = 73 : 27) illustrated the further enrichment of Rh on the frame surfaces, and a greater proportion of Rh was oxidized (Fig. S5a, ESI[†]), possibly due to the formation of a more open framework with more edge and stepped atoms.

The above route was extendable for the syntheses of trimetallic Rh–Pd–Cu and bimetallic Rh–Ni nanoframes. Pd is oxidative-etched easily in the solution of halogen ions with the addition of FeCl₃ (ref. 21) or RhCl₃.²⁶ We found that Pd and Cu in the NPs could be dissolved by HCl/O₂, despite the absence of metal ions. Fig. S8a (ESI[†]) shows that Rh–Pd–Cu NPs (Rh/Pd/Cu = 16 : 14 : 70, as measured by ICP analysis) were polyhedrons with an average size of 30.4 nm. The XRD pattern (Fig. S9, ESI[†]), HRTEM image (Fig. S10, ESI[†]) and EDS line scan profiles (Fig. S8b, ESI[†]) of NPs indicated the formation of a Rh–Pd–Cu alloy. The enrichment of Rh on the surface and enrichment of Cu in the interior appeared in Rh–Pd–Cu NPs, and the element distribution of Pd was basically like that of Cu. During the treatment of Rh–Pd–Cu NPs/C using HAC, some Cu contents were removed (Fig. S9 and S11, ESI[†]) and the value of Rh/Pd/Cu became

21 : 18 : 61. Pd atom is inclined to be oxidative-etched into a PdCl₄²⁻ complex ion under the co-existence of O₂, Cl⁻, and H⁺;²⁸ therefore, when Pd was introduced into the Rh–Cu system, the etching process of NPs was accelerated, the time of etching reduced from 9 h to 25 min and the temperature of etching reduced to 60 °C from 80 °C. The HAADF-STEM image (Fig. S8c, ESI[†]), EDS line scan profiles (Fig. S8d, ESI[†]), and TEM images (Fig. S12, ESI[†]) demonstrated the nanoframe structures of Rh–Pd–Cu NPs/C (Rh/Pd/Cu = 55 : 11 : 34).

Rh–Ni multi-twinned polyhedrons with an average size of 50.5 nm (Fig. S13 and S14, ESI[†]) and Rh–Ni porous nanoframes/C (Fig. S13, ESI[†]) were prepared by the same route. For Rh–Ni, because the standard reduction potential of Ni(n)/Ni(0) (–0.257 V) is lower than that of Cu(n)/Cu(0) (0.34 V), a higher reaction temperature (210 °C) is necessary to reduce the Ni(n) cation using OAm as the reductant. During the treatment of Rh–Ni NPs/C using HAC, more Ni content was removed due to the lower reduction potential than Cu species and the higher level of non-noble metal content (Ni/Rh = 77 : 23 vs. Cu/Rh = 63 : 37, as measured by ICP analysis). After treatment in HAC for 12 h, some microporous structure (Fig. S15, ESI[†]) appeared with corroded Ni (Rh/Ni = 38 : 62). After further etching with O₂/HCl, the Rh–Ni NPs became more porous (Fig. S13c, ESI[†]), along with a markedly increased Rh/Ni molar ratio (64 : 36).

Rh-based NPs have been known to act as efficient and selective catalysts that can readily accelerate hydrazine decomposition into hydrogen^{32,33} and have drawn much attention as hydrous hydrazine (N₂H₄·H₂O) is a promising liquid material for hydrogen storage (with a hydrogen content as high as 7.9% by weight).^{34,35} The hydrazine decomposition mainly includes two reactions: complete decomposition, H₂NNH₂ → N₂(g) + 2H₂(g) (reaction 1); and incomplete decomposition, 3H₂NNH₂ → 4NH₃(g) + N₂(g) (reaction 2). We investigated the catalytic properties of Rh–Cu NOHs/C and Rh–Cu NOHFs/C for hydrous hydrazine decomposition. For comparison, we also tested the catalytic properties of Rh/C, Cu/C, Rh_{1.7}-Cu/C catalysts prepared *via* NaBH₄ reduction (Fig. S16, ESI[†]).

As shown in Fig. 4, no evident activities were observed for carbon black or Cu/C catalysts. It was found that Rh₄Cu alloys

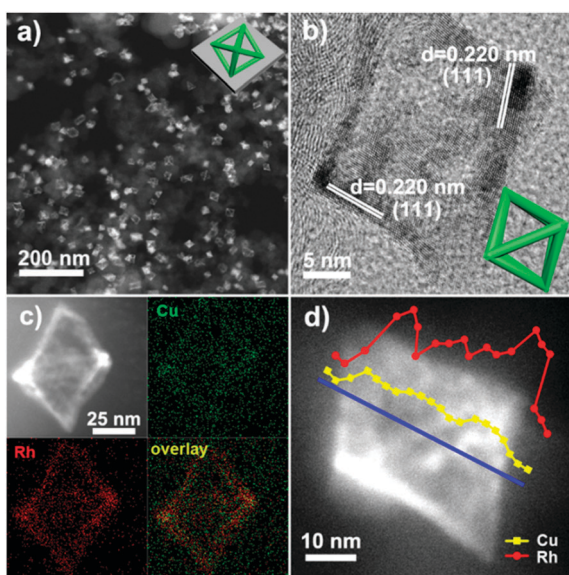


Fig. 3 HAADF-STEM image (a), HRTEM image (b), EDS elemental mapping images (c) and EDS line scan profiles (d) of Rh–Cu NOHFs/C.

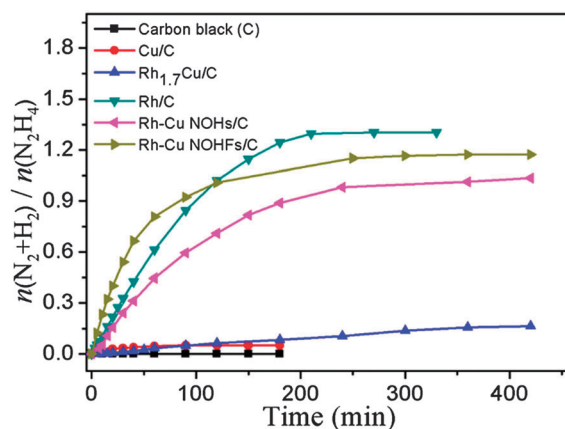


Fig. 4 Time course plots for the decomposition of hydrous hydrazine (1.0 M) in aqueous solutions over different Rh-based nanocatalysts (molar ratio: Rh/N₂H₄ = 1 : 100) and Cu/C (molar ratio: Cu/N₂H₄ = 1 : 100) at 298 K. Each data point is the average of three independent measurements.

could not catalyze hydrazine decomposition due to the negative effect of Cu,³³ and we noted that the catalytic activity of Rh_{1.7}Cu/C was very low. Interestingly, we found that Rh–Cu NOHs/C and Rh–Cu NOHFs/C could catalyze hydrazine decomposition, because of the enrichment of Rh on the surfaces, according to the XPS results. During acetic acid treatment, most of the copper atoms on the top surface layers were removed. After HCl etching, more copper atoms were removed, so the population of copper atoms on the top surface layers was much lower. According to the XPS results, for the surfaces of NOHs and NOHFs, the molar ratios of Rh/Cu were 72:28 and 88:12, respectively. The turnover frequencies (TOFs) on the basis of the data at 50% completion of hydrazine decomposition were 21.8 mol_{H₂} mol_{Rh}⁻¹ h⁻¹, 11.1 mol_{H₂} mol_{Rh}⁻¹ h⁻¹, and 33.7 mol_{H₂} mol_{Rh}⁻¹ h⁻¹ for the Rh/C, Rh–Cu NOHs/C, and Rh–Cu NOHFs/C, respectively. Compared with the Rh/C, the same amount of Rh in the Rh–Cu NOHs/C exposed much less active sites attributed to the much bigger sizes of Rh–Cu NPs. As a result, the integration between the less active sites of Rh and the negative effect of Cu led to weaker catalytic activity. We further observed that the TOF of Rh–Cu NOHFs/C was three times that of Rh–Cu NOHs/C. Rh–Cu NOHFs/C had a much higher initial reaction activity than Rh–Cu NOHs/C, even higher than Rh/C, because NPs with open structures, thin edges and higher Rh/Cu value would hold larger specific surface areas, and expose more active sites and more stepped surfaces, with the deepening of the etching process employed in this study.

As also illustrated in Fig. 4, the molar ratios between the generated H₂ and N₂ gases and the initial hydrazine were 1.30, 1.04, and 1.17 for the Rh/C, Rh–Cu NOHs/C, and Rh–Cu NOHFs/C, respectively, which corresponded to a H₂ selectivity of 36.2%, 26.5%, and 31.4%, respectively. (The H₂ selectivity could be calculated as $\chi = (3\lambda - 1)/8 [\lambda = n(\text{H}_2 + \text{N}_2)/n(\text{H}_2\text{NNH}_2)]$).³⁵ Rh–Cu NOHs/C possessed a lower H₂ selectivity than Rh/C because of the negative effects of Cu,³³ while Rh–Cu NOHFs/C possessed a slightly higher H₂ selectivity than Rh–Cu NOHs/C, and a slightly lower H₂ selectivity than Rh/C, maybe because of the reduced negative effects caused by the increasing Rh/Cu molar ratio. Before and after the first cycle of catalytic reactions, the Rh/Cu ratios were 43:57 and 43:57 for the Rh–Cu NOHs/C, 73:27 and 74:26 for Rh–Cu NOHFs/C. After four cycles of catalytic reaction, there was no obvious structural damage for Rh–Cu NOHFs/C (Fig. S17, ESI[†]), showing the robustness of the microstructure of the nanocatalysts tested during the catalytic processing.

In summary, we developed a versatile wet chemistry approach for the highly selective synthesis of Rh-based nanoframeworks, including Rh–Cu NOHFs/C, Rh–Pd–Cu nanopolyhedral frames/C, and Rh–Ni porous nanopolyhedral frames/C through preferential etching effect of 3d metals, including Cu and Ni. Due to their more accessible active sites exposed on the robust porous structure, Rh–Cu NOHFs/C showed rather higher catalytic activity for hydrazine decomposition than Rh–Cu NOHs/C at room temperature. This study has provided a powerful and practical synthetic strategy for the selective fabrication of a novel noble metal based nanoframeworks for maximizing the atomic utilization efficiency of noble metals in the nanocatalysts with high catalytic performances for many other heterogeneous catalytic reactions of wide applications.

This study was supported by the National Science Foundation of China (NSFC) (Grant No. 21025101, 21271011, and 21321001). Y.W.Z. particularly appreciates the financial aid of China National Funds for Distinguished Young Scientists from the NSFC.

Notes and references

- S. A. Maier, M. L. Brongersma, P. G. Kik, S. Meltzer, A. A. G. Requicha and H. A. Atwater, *Adv. Mater.*, 2001, **13**, 1501.
- T. A. Taton, C. A. Mirkin and R. L. Letsinger, *Science*, 2000, **289**, 1757.
- M. J. Mulvihill, X. Y. Ling, J. Henzie and P. D. Yang, *J. Am. Chem. Soc.*, 2010, **132**, 268.
- N. Tian, Z. Y. Zhou, S. G. Sun, Y. Ding and Z. L. Wang, *Science*, 2007, **316**, 732.
- Y. M. Li and G. A. Somorjai, *Nano Lett.*, 2010, **10**, 2289.
- F. Tao, M. E. Grass, Y. W. Zhang, D. R. Butcher, J. R. Renzas, Z. Liu, J. Y. Chung, B. S. Mun, M. Salmeron and G. A. Somorjai, *Science*, 2008, **322**, 932.
- Z. Y. Zhou, N. Tian, J. T. Li, I. Broadwell and S. G. Sun, *Chem. Soc. Rev.*, 2011, **40**, 4167.
- X. Q. Huang, Z. P. Zhao, Y. Chen, C. Y. Chiu, L. Y. Ruan, Y. Liu, M. F. Li, X. F. Duan and Y. Huang, *Nano Lett.*, 2014, **14**, 3887.
- V. R. Stamenkovic, B. Fowler, B. S. Mun, G. F. Wang, P. N. Ross, C. A. Lucas and N. M. Markovic, *Science*, 2007, **315**, 493.
- D. S. Wang and Y. D. Li, *Adv. Mater.*, 2011, **23**, 1044.
- S. J. Hwang, S. K. Kim, J. G. Lee, S. C. Lee, J. H. Jang, P. Kim, T. H. Lim, Y. E. Sung and S. J. Yoo, *J. Am. Chem. Soc.*, 2012, **134**, 19508.
- Y. G. Sun, B. Mayers and Y. N. Xia, *Adv. Mater.*, 2003, **15**, 641.
- J. Erlebacher, M. J. Aziz, A. Karma, N. Dimitrov and K. Sieradzki, *Nature*, 2001, **410**, 450.
- M. McEachran, D. Keogh, B. Pietrobon, N. Cathcart, I. Gourevich, N. Coombs and V. Kitaev, *J. Am. Chem. Soc.*, 2011, **133**, 8066.
- B. Y. Xia, H. B. Wu, X. Wang and X. W. Lou, *J. Am. Chem. Soc.*, 2012, **134**, 13934.
- X. Hong, D. S. Wang, S. F. Cai, H. P. Rong and Y. D. Li, *J. Am. Chem. Soc.*, 2012, **134**, 18165.
- C. Chen, Y. J. Kang, Z. Y. Huo, Z. W. Zhu, W. Y. Huang, H. L. L. Xin, J. D. Snyder, D. G. Li, J. A. Herron, M. Mavrikakis, M. F. Chi, K. L. More, Y. D. Li, N. M. Markovic, G. A. Somorjai, P. D. Yang and V. R. Stamenkovic, *Science*, 2014, **343**, 1339.
- S. B. Wang, W. Zhu, J. Ke, J. Gu, A. X. Yin, Y. W. Zhang and C. H. Yan, *Chem. Commun.*, 2013, **49**, 7168.
- H. Zhang, M. S. Jin, H. Y. Liu, J. G. Wang, M. J. Kim, D. R. Yang, Z. X. Xie, J. Y. Liu and Y. N. Xia, *ACS Nano*, 2011, **5**, 8212.
- Y. E. Wu, D. S. Wang, G. Zhou, R. Yu, C. Chen and Y. D. Li, *J. Am. Chem. Soc.*, 2014, **136**, 11594.
- S. F. Xie, N. Lu, Z. X. Xie, J. G. Wang, M. J. Kim and Y. N. Xia, *Angew. Chem., Int. Ed.*, 2012, **51**, 10266.
- Y. G. Sun and Y. N. Xia, *Science*, 2002, **298**, 2176.
- Z. M. Peng, H. J. You, J. B. Wu and H. Yang, *Nano Lett.*, 2010, **10**, 1492.
- Y. Yuan, N. Yan and P. J. Dyson, *ACS Catal.*, 2012, **2**, 1057.
- S. F. Xie, H. C. Peng, N. Lu, J. G. Wang, M. J. Kim, Z. X. Xie and Y. N. Xia, *J. Am. Chem. Soc.*, 2013, **135**, 16658.
- B. T. Sneed, C. N. Brodsky, C. H. Kuo, L. K. Lamontagne, Y. Jiang, Y. Wang, F. Tao, W. X. Huang and C. K. Tsung, *J. Am. Chem. Soc.*, 2013, **135**, 14691.
- V. Mazumder and S. H. Sun, *J. Am. Chem. Soc.*, 2009, **131**, 4588.
- M. C. Liu, Y. Q. Zheng, L. Zhang, L. J. Guo and Y. N. Xia, *J. Am. Chem. Soc.*, 2013, **135**, 11752.
- Y. E. Wu, D. S. Wang, Z. Q. Niu, P. C. Chen, G. Zhou and Y. D. Li, *Angew. Chem., Int. Ed.*, 2012, **51**, 12524.
- L. Gan, M. Heggen, R. O'Malley, B. Theobald and P. Strasser, *Nano Lett.*, 2013, **13**, 1131.
- C. H. Cui, L. Gan, M. Heggen, S. Rudi and P. Strasser, *Nat. Mater.*, 2013, **12**, 765.
- S. K. Singh, X. B. Zhang and Q. Xu, *J. Am. Chem. Soc.*, 2009, **131**, 9894.
- S. K. Singh and Q. Xu, *J. Am. Chem. Soc.*, 2009, **131**, 18032.
- L. He, Y. Q. Huang, A. Q. Wang, X. D. Wang, X. W. Chen, J. J. Delgado and T. Zhang, *Angew. Chem., Int. Ed.*, 2012, **51**, 6191.
- X. H. Xia, L. Figueroa-Cosme, J. Tao, H. C. Peng, G. D. Niu, Y. M. Zhu and Y. N. Xia, *J. Am. Chem. Soc.*, 2014, **136**, 10878.